Journal of Molecular Structure 1188 (2019) 205–213

Contents lists available at ScienceDirect

Journal of Molecular Structure

journal homepage: http://www.elsevier.com/locate/molstruc

Application of X-ray absorption spectroscopy for L_3-edges of Dy and Yb in dibenzoylmethanide complexes: Experiment and theoretical interpretation

Aleksandra Yu. Andreeva [a], Ilia A. Pankin [b, c, *], Taisiya S. Sukhikh [a, d], Antonina N. Kravtsova [b], Sergey N. Konchenko [a, d], Svetlana G. Kozlova [a, d], Alexander V. Soldatov [b]

[a] Nikolaev Institute of Inorganic Chemistry of SB RAS, Novosibirsk, Russia
[b] The Smart Materials Research Center, Southern Federal University, Sladkova 178/24, 344090, Rostov-on-Don, Russia
[c] Department of Chemistry and NIS Interdepartmental Center, University of Torino, via Giuria 7, I-10125 Torino, Italy
[d] Novosibirsk State University, Novosibirsk, Russia

ARTICLE INFO

Article history:
Received 31 January 2019
Received in revised form
17 March 2019
Accepted 19 March 2019
Available online 26 March 2019

Keywords:
Polynuclear lanthanide complexes
XANES
Local atomic structure
Electronic structure
DOS analysis

ABSTRACT

Local atomic and electronic structure of Dy- and Yb-based dibenzoylmethanide complexes has been investigated by analysis of experimental and theoretical L_3-edge XANES spectra. The local atomic structure similarity between recrystallized and as-synthesized samples has been proved by XANES. Differences in the experimental XANES spectra collected for a Ln-complexes with a different ligand ratio (dbm^-): (O-btd^-) have been observed and assigned with a higher abundancy of elongated Ln-N bonds with respect to Ln-O for the sample where Ln-ions coordinated by higher number of O-btd^- ligands. In this work we also critically discussed XANES simulations based on monoelectronic approach as implemented in FDMNES code for L_3-edge spectra calculated for Ln-complexes. Density of electronic state calculation has been performed in order to elucidate the origin of the XANES features. Since the product yield of as-synthesized Ln-complexes is significantly higher rather than after re-crystallization this work demonstrate a high potential of DFT-assisted XANES analysis for the structural investigation of as-synthesized complexes without long-range atomic ordering.

1. Introduction

Over a last years many research efforts have been dedicated for lanthanide compounds (Ln) due to their promising and actual applications. Due to the unique photophysical [1,2] and magnetic properties [3,4], these compounds and their derivatives found an application in sensors [1,5] and solar cell [1,6] development and biomedical analysis as well [5]. Because some of the Ln-based compounds possess a molecular magnet behavior exhibiting magnetic memory effect, a particular interest on potential using as a high-density information storage media has been attracted [7–9].

Among lanthanide-based materials a particular attention is given to lanthanide molecular complexes with 8-quinolinolate and β-diketonate ligands because of their antenna effect on the Ln (III) exhibit near infra-red (NIR) luminescence [2,10]. 2,1,3-benzothiadiazole derivatives attract current attention because of their potential utilization in the design and synthesis of organic light-emitting diodes (OLEDs) [10,11] being also considered as the ligands for transition metal complexes [12]. In our previous work, we have reported a synthetic routes and comprehensive crystal structure characterization of NIR-emissive hetero ligand tetranuclear Er-based [11] and further Dy- and Yb-based [13] complexes with dibenzoylmethanide (**dbm**) and 4-hydroxo-2,1,3-benzothiadiazolate (**O-btd**) ligands. The latter has been proposed to be a good antenna ligand for Er [11] and (Yb,Dy) ions [13] in corresponding tetra-nuclear complexes. Thus, the difference in the (**dbm^-**)/(**O-btd^-**) ratios in the synthesized complexes has been found to play a crucial role in the NIR emitting properties of the samples.

* Corresponding author. The Smart Materials Research Center, Southern Federal University, Sladkova, 178/24, 344090, Rostov-on-Don, Russia.
E-mail address: ipankin@unito.it (I.A. Pankin).

https://doi.org/10.1016/j.molstruc.2019.03.073
0022-2860/

The current work is aimed to show a high potential of the X-ray absorption spectroscopy (XAS) for study of local atomic and electronic structures of Ln-based complexes. Being element-selective and local technique XAS spectroscopy can be applied for the study of local atomic structure of non-crystalline or microcrystalline solids without long-range atomic order where a single-crystal X-ray diffraction (XRD) cannot be employed. In this context, we study powder samples of dibenzoylmethanide complexes [Ln_4 $(dbm)_4(O\text{-}btd)_6(OH)_2$] (**1a** for Ln = Yb and **1b** for Ln = Dy) [Ln_4 $(dbm)_6(O\text{-}btd)_4(OH)_2$] (**2a** for Ln = Yb and **2b** for Ln = Dy). They structure were previously characterized by XRD [13] as THF or toluene solvates, which were prepared *via* recrystallization of unsolvated powder compounds. The latter have the same composition, but their long-order arrangement is supposed to be different due to lack of the solvate molecules. However, we assumed that the local geometry of the unsolvated and solvated complexes is similar. To confirm this hypothesis, we present here the investigation of atomic and electronic structure by utilization of the XANES spectroscopy above L_3 edge of Ln (Dy, Yb, Sm) in tetranuclear complexes, supported by DFT-assisted XANES simulations.

The nature of L_3 absorptions edge of transition metals explain usually observed a much sharper shape of the white line peak (the most intensive absorption resonance in the spectra; hereinafter referred to as "WL peak") as compared to the K edges which correspond to transitions from 1*s* core orbitals to typically delocalized 2*p*-states [14]. The same sharp and intensive WL peaks are observed also for L_3 spectra of lanthanides and changes of their energy localization could be employed in order to estimate changes in the oxidation states of Ln-atoms [15,16]. An oxidation states can be also estimated by the appearance of multi-electron excitations in the XANES spectra assigned to electronic configuration variations in 4*f* shell *via* screening effects and charge transfer excitations [17–21]. For L_3 edge XANES spectroscopy, a direct transition to the 4*f* is forbidden due to dipole selection rule ($\Delta l = \pm 1$), however some works reported a weak feature observed on the low energy slope of the main L_3 absorption resonance and attributed to $2p \rightarrow 4f$ quadrupole transitions [18,22]. On the example of Ce(IV) oxide it has been shown by Soldatov et al., [23] that L_3 pre-edge region is mostly contributed by *d*-states rather than by $2p \rightarrow 6s$ transitions, as their intensity has been found negligible by implementation of full multiple scattering calculations.

An optimization of theoretical approach for the simulation of L edges in transition metal complexes as well as other compounds with strongly correlated electrons is a well-known challenge. A several ways for a proper description of the spectral features in such kind of systems which require many body corrections have been discussed by A. Guda et al. [24]. Ab-initio multiple-scattering (MS) theory based code FEFF 9.5 [25] has been found as an efficient way to simulate L_3 XANES and L_3-RIXS spectra for actinide and lanthanide compounds and successfully reproduce both dipole and quadrupole transitions in the same spectrum [26]. Moreover a successful utilization of FDMNES code [27] (where both finite difference method and multiple scattering (MS) theory is implemented) has been shown recently for the theoretical modeling of $L_{2,3}$ absorption edges in 4*f*-5*d* systems, in particular for Re-based reference compounds [28] or anti-ferroquadrupolar NdMg [29] and even in 5*f*-6*d* systems for U in various valence states [26].

In the present work the theoretical approach based on one-electron approach as implemented in FDMNES code (See Section 2.3) employed for L_3 XANES simulations of Ln-based materials is critically discussed. The same experimental and theoretical XAS methods were applied to model Ln_2O_3 and [Ln_5 $(dbm)_{10}(OH)_5$] (Ln = Dy, Yb) compounds of known crystal structure for comparison.

2. Experiment details and theoretical approaches

2.1. Synthesis of materials

In the present work, two types of tetranuclear complexes containing $(O\text{-}btd)^-$ and $(dbm)^-$ ligands, namely [Ln_4 $(dbm)_4(O\text{-}btd)_6(OH)_2$] (**1a** for Ln = Yb and **1b** for Ln = Dy) and [Ln_4 $(dbm)_6(O\text{-}btd)_4(OH)_2$] (**2a** for Ln = Yb and **2b** for Ln = Dy) have been investigated by X-ray absorption spectroscopy (Ln_2O_3 and [Ln_5 $(dbm)_{10}(OH)_5$] (**3a** for Ln = Yb and **3b** for Ln = Dy) have been used as well for comparative analysis). They have been prepared by previously reported synthetic procedures [11]. This approach is actually divided into two synthesis routes. The first one based on the reaction of OH-btd and dibenzoylmethane (H-dbm) with chloride of lanthanides $LnCl_3 \cdot 6H_2O$ in the presence of organic base. The second approach is based on the ligand substitution reaction between $(O\text{-}btd^-)$ and the pentanuclear complexes [Ln_5 $(dbm)_{10}(OH)_5$], the latter in turn being prepared from the same precursor $LnCl_3 \cdot H_2O$. A details of synthesis procedure of Ln-tetranuclear complexes as well as a possible products along with crystallization procedure and single-crystal diffraction based structural characterization are presented in detail in our previous works [11,13]. Hereinafter, **1**, **2** and **3** names are for [Ln_4 $(dbm)_4(O\text{-}btd)_6(OH)_2$] [$Ln_4$ $(dbm)_6(O\text{-}btd)_4(OH)_2$] and [$Ln_5$ $(dbm)_{10}(OH)_5$] families of the complexes respectively.

2.2. X-ray absorption experiment and sample preparation

X-ray absorption data were collected by using laboratory spectrometer Rigaku R-XAS Looper. The measurement of Ln (where Ln = Dy and Yb) L_3-edge XANES spectra has been performed in conventional transition mode. The powder samples were mixed with a buffer compound BN (almost transparent material in a hard X-ray range) and consistently grinded in the chemical mortar before being pressed in the form of self-supported pellets of the optimized thickness with a surface area around 1.3 cm^2. A mixing with a buffer compound is necessary to get as high as possible homogeneous sample and optimized absorption jump because it has a crucial effect on the data quality in the condition of the low intense X-ray beam (namely using X-ray tube a source of incident beam).

X-ray tube equipped by Mo anode and LaB_6 cathode was used as an X-rays source of the spectrometer. The accelerated voltage and tube current were set up as 17 kV and 70 mA, respectively. The monochromator and collimation slits were mounted in the Rolland geometry which allow effectively focus an X-ray beam on the sample while consistent motion of an X-ray tube and monochromator. Bent-shaped Johansson type Ge (311) crystal (2 d = 3.4120 Å) was used to obtain a monochromatic beam in the range from 6500 eV to 9400 eV with an energy resolution around 3.5–4.0 eV. Gas chamber detector filled with Ar under 300 mbar was employed as I_o counter to monitor the intensity of accident X-ray beam (absorb around 10–15% of X-rays in the above-mentioned energy region). To measure the transmitted intensity of X-ray beam, the scintillation detector (SC-70) has been utilized. To get better signal-to-noise ratio, 3 to 5 measurements were performed which were subsequently averaged for each sample.

For Dy-based samples, EXAFS data acquisition was also performed. An EXAFS scans were collected up to 10–12 $Å^{-1}$ *k*, depending of the sample homogeneity and observed edge jump. From 3 to 4 measurements has been averaged in order to get a reasonable signal-to-noise ratio.

2.3. Theoretical approach for XANES simulations

XANES simulations has been performed by finite difference method using full potential and multiple scattering (MS) theory approach using restricted muffin-tin potential [30] as implemented in FDMNES software [27]. The code originally represents a one-electron approach and is fully relativistic and thus, takes into account the spin-orbit coupling in both core state and optionally in the final states. The ab-initio calculations were carried out in the real space using clusters built around each nonequivalent x-ray absorbing atom. The code is based on the ab-initio calculations of the electronic structure and further solving of the Schrodinger equation (discretized radial Schrodinger equation when the finite difference method approach is used) in the finite number of the grid points in a real space where the atomic potential is determined by superposing the self-consistent atomic potentials [31]. In the present work, the exchange-correlation potential was constructed using Hedin-Lunquist formulation. Recent improvement [32] of the code based on implementation of Sparse solvers for the finite difference matrix (which permits to solve systems of linear equation with sparse matrices) provides a significantly faster calculation and allows to perform previously demanding XANES simulations for a large systems. In the present work, XANES spectra were calculated for an atomic cluster with a size determined by a radius of 6 Å centered on the absorbing atom. The position of Fermi level was estimated for a non-excited system within a cluster of smaller radius 3.5 Å. To compare with the experimental data, the convolution procedure was performed to account for a life-time broadening of Ln (Dy, Yb) L_3 edges. For the models consisting a different nonequivalent absorbing atoms a final theoretical spectrum has been obtained by weighted averaging.

3. Results and discussions

3.1. Experimental study

Tetranuclear complexes under the study, *viz*. [Ln_4 $(dbm)_4(O\text{-}btd)_6(OH)_2$] (**1a** for Ln = Yb; **1b** for Ln = Dy and **1c** for Ln = Sm) and [Ln_4 $(dbm)_6(O\text{-}btd)_4(OH)_2$] (**2a** for Ln = Yb and **2b** for Ln = Dy) underwent recrystallization from THF or toluene resulting in the formation of **1**·6 THF and **2**·$7C_7H_8$. The latter has been previously characterized by XRD previously [11]. According to XRD, the complexes are centrosymmetric and contain the $Ln_4(OH)_2$ core, similar to all the samples under the study. Within this core, four Ln (III) ions define a parallelogram and are bridged by two μ_3-OH groups, which are located on both sides of the metal plane. In the recrystallized complexes, ten organic ligands coordinated to the metal centers, resulting in a distorted square-antiprismatic geometry for each Ln ion (See Fig. 1).

In the present work, as-synthesized powdered non-solvated samples of different structure due to lack of the solvate molecules were studied. In fact, the yield of as-synthesized compounds **1**–**2** was good (70–90%); however, after recrystallization with formation of **1**·6 THF and **2**·$7C_7H_8$ it dropped to 3–5%. Thus, it is better to use non-solvated complexes for further studies. To prove that the local geometry of the unsolvated and solvated complexes is similar, atomic and electronic structure of the compounds **1**–**2** was studied using XANES spectroscopy supported by DFT-assisted XANES simulations. Ln_2O_3 and pentanuclear complexes [Ln_5 $(dbm)_{10}(OH)_5$] (Ln = Dy, Yb [4]) of known crystal structure were also studied for a comparison.

Fig. 2 reports an experimental XANES spectra collected at Dy L_3-edge for the complexes **1b** and **2b** in comparison with the experimental curves collected for Dy_2O_3 and [Dy_5 $(dbm)_{10}(OH)_5$] (**3b**) [4]. As it was discussed above (please see Introduction section) the L_3 edge XANES spectra of Dy compounds characterized by sharp and intensive WL peak (denoted as feature A in the Fig. 2) mostly assigned to dipole allowed $2p_{3/2} \rightarrow 5d_{3/2}$ electronic transitions induced by absorption of incoming X-ray photons. A possible quadrupole $2p \rightarrow 4f$ transitions for $L_{2,3}$ edges of lanthanides observed in XAS, HR-XANES and RIXS spectra [17,26,29] are virtually beyond the detection limit of laboratory Rigaku R-XAS spectrometer.

A smoothed feature located on the high energy slope of the WL peak is observed for Dy-complexes, while at the spectrum of a model compound Dy_2O_3 a well distinguishable peak has been observed (denoted as feature B in the Fig. 2). In the higher energy region, well-defined absorption resonance peak C and smoothed hump (denoted as feature D) are observed both for Dy_2O_3 and all Dy-complexes under study. The main differences in the experimental spectra of the Dy-complexes and Dy_2O_3 are the following: (i) intensity of the WL peak is higher for the complexes; (ii) the feature B (located between features A and C) for Dy_2O_3 manifests itself as a well distinguishable peak, while for the complexes it is smoothed; (iii) the peak C is significantly shifted (by ca. 3.1 eV) towards the lower energy region for Dy-complexes (peak C energy position in Dy-complexes – 7827.5 eV). The latter could be due to an elongated averaged Dy-O distances in Dy-complexes with respect to Dy-O distances that in the 1st coordination shell of Dy_2O_3 in accordance with a Natoli's rule [33]; however, a symmetry preservation in the local atomic proximity of absorber is necessary. Whereas the intensity and sharpness of WL peak of L_3 edge should correlate with an availability and energy localization of unoccupied 5*d* valence orbitals of Dy ions. The differences in the spectra of different tetranuclear complexes **1b** and **2b** are discussed below in detail.

To estimate Dy-O distances in the complexes in comparison with Dy_2O_3, a k^2-weighted ($k^2\chi(k)$) Fourier transformed EXAFS amplitudes were analyzed (Fig. 3). Because of the signal quality a direct Fourier transformation of the background subtracted EXAFS signal has been performed in a relatively short range in *k* space from 2.90 Å to 9.50 Å. As a first coordination shell in the crystallized analogue of investigated Dy-complexes is represented in total by eight O and N atoms located at different distances from absorber only qualitative analysis is reasonable due to a large number of structural parameters from the one side and lack of independent point in the EXAFS data from the other side.

Fourier transformed EXAFS amplitudes of Dy_2O_3, **2b** and **3b** characterized by the first coordination shell maxima located in R range from 1.1 Å to 2.3 Å. This feature is mostly associated with a single scattering Dy-O and both Dy-O and Dy-N paths for Dy_2O_3 and Dy-complexes, respectively. In the higher R-region, a well-defined doublet peak located at 2.8 Å – 4.1 Å is observed only for Dy_2O_3. This second shell maxima observed for Dy_2O_3 is assigned to higher Dy-O shells and Dy-Dy scattering events contribution. For the complexes, this region is at almost noise level intensity, most likely due to the significantly lower quality of the signal with respect to Dy_2O_3. The first shell maxima of k^2-weighted FT-EXAFS phase uncorrected amplitudes for **2b** (1.89 Å) are observed at slightly higher R values (See Fig. 3a) with respect to **3b** and Dy_2O_3 (1.83 Å and 1.84 Å, respectively). Thus, one could assume a slightly shorter averaged Dy-O distances in **2b** with respect to **3b**. However more informative imaginary part of FT $k^2\chi(k)$ signal demonstrate that the averaged Dy-O distances are expected to be similar for **2b** and **3b**, while the distances in Dy_2O_3 are slightly longer. It should be emphasized that all these assumptions are mostly presumptive and for a proper quantitative analysis of the EXAFS spectra, a better-quality signal collected at higher *k* values in conjunction with an EXAFS fitting routine are required.

Fig. 4 shows an experimental XANES spectra collected at Yb L_3-

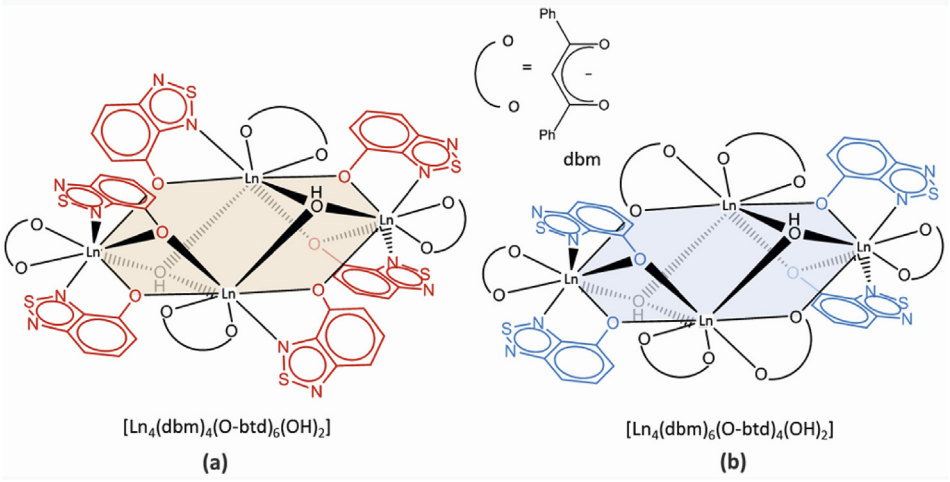

Fig. 1. Schematic representation of the single-crystal XRD structures of **1a**·6 THF (a) and **2a**·7C_7H_8 (b) described in detail in Ref. [11].

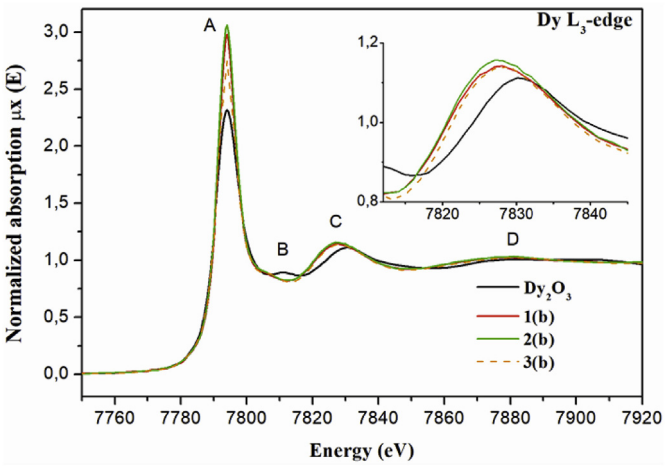

Fig. 2. Experimental Dy L_3-edge XANES spectra of the complexes **1b**, **2b** and **3b** in comparison with Dy_2O_3. The inset shows magnifications of the second main absorption resonance denoted as a feature C.

edge for the complexes **1a**, **2a** and **3a** in comparison with Yb_2O_3. Yb L_3-edge spectra reflect the same features in shape of the spectra which were discussed for Dy L_3-edge XANES dataset. Different intensity of WL peak follows the same trend observed for Dy-complexes, but exhibits higher variety between the complexes **1a**, **2a** and **3a** comparing to **1b**, **2b** and **3b**. Also changes in the second main absorption resonance peak intensity (denoted as peak C at Figs. 2 and 4) being observed even more explicitly for Yb-based complexes allows us to emphasize a difference between Ln-tetranuclear (Ln = Dy, Yb) complexes having different (dbm^-):($O\text{-}btd^-$) ligand ratio. In addition, for Yb compounds, high-energy feature D appears to be more intensive and more distinguishable with respect to Dy compounds.

At the same time, an energy difference for features C between the complexes (centered at 8981.3 eV) and Yb_2O_3 (centered at 8983.9 eV) is close to that for Dy compounds. The nature of the spectral features and their relative intensities for two tetranuclear complexes **1a** and **2a** are discussed below (See Section 3.2).

Finally, the energy position of the absorption edge in the L_3-edge XANES spectra can be applied for the estimation of an oxidation

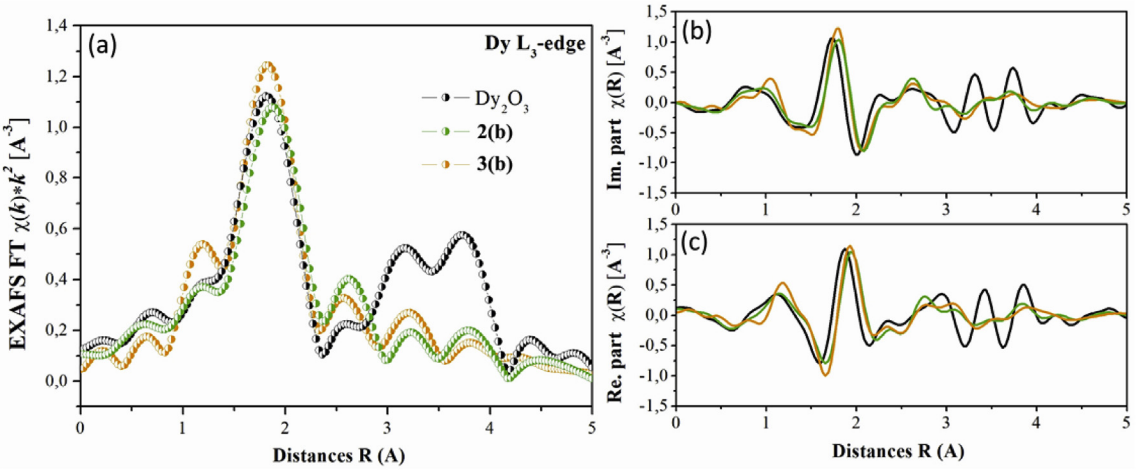

Fig. 3. Phase uncorrected Dy L_3-edge experimental **(a)** k^2-weighted Fourier transformed EXAFS amplitudes, **(b)** imaginary and **(c)** real part of Fourier transformed EXAFS signals collected for the complexes **2b** and **3b** in comparison with Dy_2O_3.

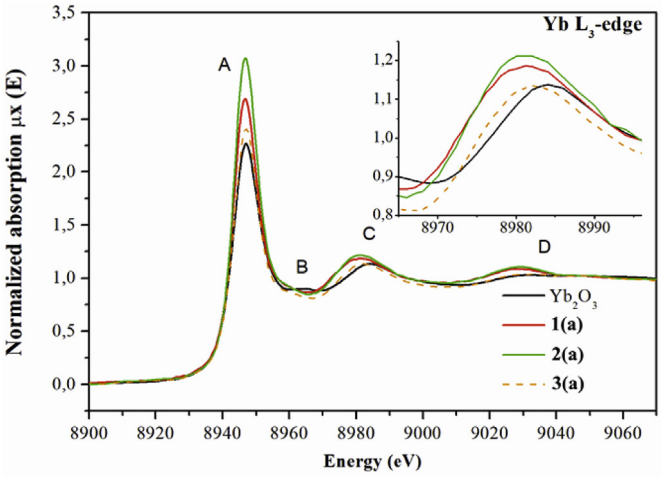

Fig. 4. Experimental Yb L_3-edge XANES spectra of the complexes **1a**, **2a** and **3a** in comparison with Yb_2O_3. The inset shows magnifications of the second main absorption resonance denoted as a feature C.

states in lanthanides and actinides. In the present work an oxidation state for Dy and Yb ions in both tetranuclear and pentanuclear complexes has been estimated to be equal to +3 by direct experimental approach, namely by comparing an energy position of the absorption edges in L_3 XANES spectra with a model compounds: Dy_2O_3 for Dy L_3-edge and Yb_2O_3, $YbCl_3$, YbF_3 for Yb L_3-edge (see Figure S2 in Supplementary materials). These results are in line with our previous findings [13], where an oxidation state of Ln ions has been determined by the fact that an effective magnetic moment (μ_{eff}) calculated for a system of four non-interacting Ln (III) ions in the ground state (belonging to $Ln_4(OH_2)$ core) provides a good agreement with experimentally determined μ_{eff} derived from magnetic suppressibility $\chi(T)$ experimental dataset (the same procedure was successfully applied for isostructural Er-tetranuclear complexes [11]).

Indeed, it is obvious that one could expect +3 oxidation state of Ln-ions accounting for a synthesis route (i.e. using an $LnCl_3$ as an initial reagent) and in fact changes of oxidation state may take place only in the presence of strong reductive agents [34].

3.2. XANES theoretical modeling

As discussed above, difference in experimental Ln L_3-edge XANES spectra was observed for tetranuclear Dy and Yb complexes with a different (dbm^-): ($O\text{-}btd^-$) ligand ratio. Taking into account our previous finding [13], this (dbm^-): ($O\text{-}btd^-$) ligand ratio in crystallized complexes plays a crucial role in optical properties [13,35] of the system revealing that ($O\text{-}btd^-$) ligand can be considered as an efficient antenna for NIR luminescence. To shed light on atomic and electronic structural insights of the complexes, XANES spectra were simulated.

A priori finite difference method in full potential approximation is supposed to be more precise, but at the same time needs more computational resources in comparison with multiple scattering (MS) theory approach. Therefore, finite difference method was chosen first to examine acceptability of FDMNES code (See Section 2.3) for the Ln L_3-edge XANES simulation. The spectra of model compounds Dy_2O_3 and Yb_2O_3 were calculated first (the simulation results for Dy_2O_3 reported at Figure S3 in Supplementary materials). In order to compare a theoretically obtained spectra with an experimental data, simulated spectra have been further convoluted by implementing a routine as a part of FDMNES code to account for core-hole life-time broadening as well as monochromator energy resolution (convolution parameters test for Dy_2O_3 reported at Figure S4 in Supplementary materials). In both cases, a reasonable agreement has been obtained. All the features observed in the experimental spectra are reproduced in the simulated ones; however, the energy gap between the WL peak (feature A) and higher-energy spectral features (B, C and D) is underestimated. For instance, the energy position of the feature C is underestimated by ~ 4.53 eV.

Then, XANES spectra for tetranuclear Dy and Yb complexes **1**–**2** as well as pentanuclear compounds **3** were simulated. The latter has been simulated in order to verify experimentally observed trend of WL peak damping for a pentanuclear complexes. The results of XANES simulations using finite difference method approach (hereinafter referred to as "FDM approach") are presented in Fig. 5 in comparison with the experimental data. For all Dy- and Yb- L_3-edge theoretical XANES spectra, the convolution procedure with the same set of parameters for each lanthanide absorbing atom (optimized in order to get a better agreement with the experimental data) has been employed.

All spectral features of the L_3-edge XANES spectra experimentally observed for tetranuclear and pentanuclear complexes and the shape of the L_3-edge XANES spectra et all have been successfully reproduced by FDM approach. However, for the pentanuclear complexes **3a**, theoretically obtained WL peak intensity appears significantly more intensive with respect to tetranuclear ones **1a, 2a**. Indeed, a local atomic structure of Ln-atoms in pentanuclear complexes should be more symmetric with respect to tetranuclear ones because for the tetranuclear Ln-complexes one expected a presence of at least one nitrogen atomic ligand having an elongated Ln-N distances with respect to Ln-O distances. This could result in more localized *d*-states in pentanuclear complexes, which mostly determine the shape of the XANES spectra as it revealed by the DOS analysis presented below (see Section 3.4). The lower intensity of the WL peak for pentanuclear complexes in contrast to observed in experimental spectra can be explained by the fact that in as-synthesized **3a** and **3b** complexes the coordination sphere of Ln ions undergoes a higher disordering as compared to tetranuclear ones and to the XRD determined structure used for simulations.

The energy position of second absorption maxima C in the calculated spectra are underestimated with respect to the experimental one. The differences in the energy are *ca.* 2.9 eV for Dy L_3-edge and *ca.* 3.4 eV for Yb L_3-edge. From one side, this can be due to the differences in the structure of studied non-solvated and solvated (for which the structure was derived by XRD) compounds. Better fit of experimental data can be achieved using artificially shortened distances in the molecules by 1, 2, 3, 4 and 5% (corresponding models were obtained by isotropic compression of the unit cells). The results of the simulations are available in Supplementary materials (See Figure S5). However, the XANES simulations for Ln-oxides with a well-known structure and further comparison with an experimental spectrum demonstrates the same trend in underestimation of energy position for peak C. Thus, energy position discrepancy means that when the FDM simulated spectra is compared with experimental L_3-XANES spectra collected for the Ln-complexes and the energy position of the second absorption maxima (feature C) is fitted in order to match with experimental peak one could expect an underestimation of the interatomic distances in proximity of Ln-ions.

3.3. Comparison of XANES spectra for the $[Ln_4(dbm)_4(O\text{-}btd)_6(OH)_2]$ and $[Ln_4(dbm)_6(O\text{-}btd)_4(OH)_2]$ complexes

Relative intensities of WL peak (feature A) and second main absorption peak (feature C) are perfectly reproduced for

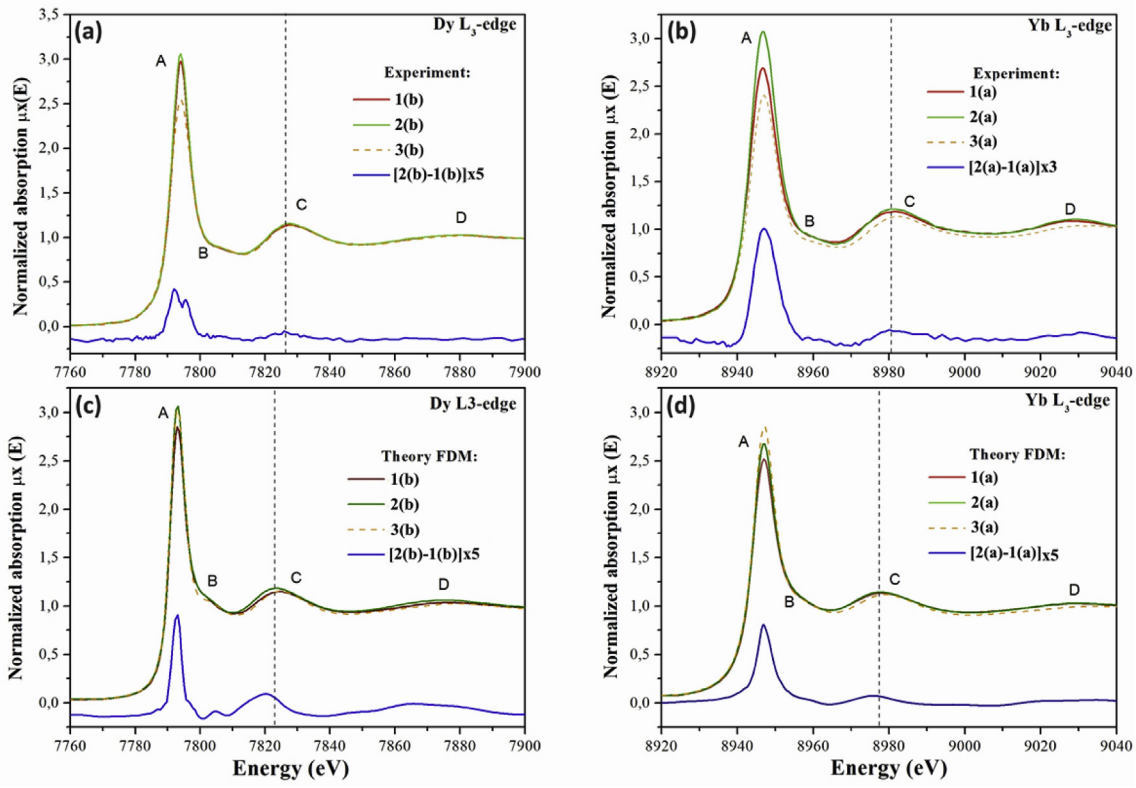

Fig. 5. Experimental **(a,b)** and theoretical **(c,d)** L_3-edge XANES spectra for tetranuclear and pentanuclear complexes and magnified differential (**2**–**1**) XANES spectra .Vertical dotted lines represent an averaged (for two different tetranuclear complexes) energy position of second absorption maxima C.

tetranuclear complexes. Thus, these features are obviously assigned with differences in the local atomic and electronic structures for the complexes with different ligand ratios. The experimental difference (**2**–**1**) XANES spectra (Fig. 5) emphasize greater changes for Yb samples comparing to Dy ones; however, FDM simulated spectra are close with slightly higher differences for Dy complexes in the region of feature C comparing to Yb ones. It is important to note that theoretical differential curves clearly demonstrate for both Dy and Yb cases that not only changes in the second absorption peak intensity (feature C) is observed for the complexes coordinated by different number of (dbm^-) ligands, but an energy shift towards the lower energy for those coordinated by six (dbm^-) ligands.

The feature C in the experimental differential XANES spectra is less pronounced due to the restricted experimental resolution but also a higher extent of structural disordering of as-synthesized complexes with respect to the models of recrystallized complexes used for XANES simulations (the schematic representation of the structure is shown in Fig. 1).

A possible explanations of higher WL peak (feature A) for the compounds **2** comparing to **1** and second main absorption maxima (feature C) as well as its slight energy shift (reflected more obviously in the theoretical XANES spectra) arises from the structural differences of tetranuclear complexes. In fact, the first coordination sphere of the complexes **1** and **2** differs by one O or N atom coordinated to the one of Ln atoms (see Fig. 6 on the example of Ln = Yb). The averaged Ln-N (Ln = Dy, Yb) bond lengths of 2.55 Å and 2.53 Å, (for Dy and Yb complexes respectively) are longer than an averaged Ln-O bond length of 2.34 Å and 2.31 Å in the complexes (See Table 1).

The presence of N atom in a position of O atom in the first coordination sphere of Ln results in higher local distortion in **1** complexes (6 O-btd ligands), while one of two inequivalent Ln ion in **2** complexes (4 O-btd ligands) is coordinated solely by O-ligands (for the table of interatomic distances in the first coordination sphere of Ln-ion in investigated complexes please see Table 1 and Tables S1–S3 in Supplementary materials). This structural distortion affects the electronic structure of *d*- valence Ln orbitals, resulting in a slightly more delocalized 5*d*-states for complexes containing one additional N atoms in Ln coordination. The energy shift of the peak C observed in unconvoluted spectra calculated for $Yb^{(1)}$ (coordinated by 6 O and 2 N atoms) and $Yb^{(2)}$ (coordinated by 8O atoms) for **2a** support the above provided explanations (see Figure S6 in Supplementary materials).

Since L_3-edge Ln XANES spectra almost coincide with a density of *d*-unoccupied state (as revealed in the Section 3.4: *DOS analysis*), these delocalization phenomena obviously will affect the XANES shape, resulting in less intensive (more broaden) spectral features. This apparently can be found as an explanation of the different WL peak intensity observed for complexes with four and six (dbm^-) ligands.

3.4. Partial density of states (DOS) analysis

Fig. 7 shows an unconvoluted contributions by $Yb^{(1)}$ crystallographic nonequivalent positions to the theoretical Yb L_3-edge XANES spectra calculated for **1a** model and simulated averaged density of electronic *p*-states of the atoms of the first coordination sphere. The latter are represented by one N and seven O atoms denoted as O(s), O(d) and O(t) bonded to one (s-single), two (d-double) and three (t-triple) Yb ions of $Yb_4(OH)_2$ core, respectively. The analysis of the calculated partial density of states (DOS) reveals that the features observed in the experimental XANES spectrum are mostly assigned to the density of *d*-unoccupied states of absorbing $Yb^{(1)}$ ion: they almost perfectly resemble the shape of simulated for

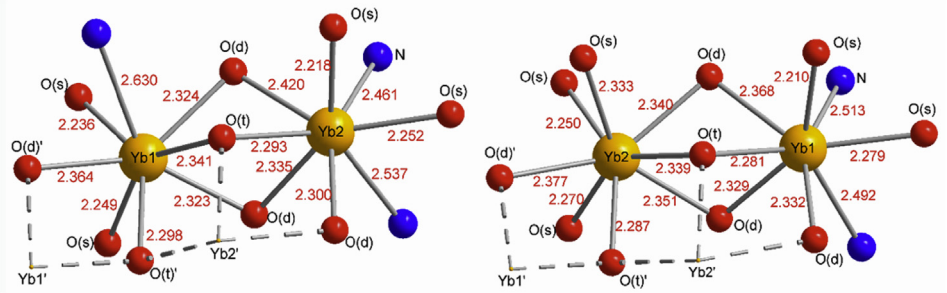

Fig. 6. The first coordination sphere of two crystallographically non-equivalent Yb atoms of the complexes **1a** (left) and **2a** (right). Atom labels having ‘ refer to symmetry-generated atoms.

Table 1
Interatomic distances in the first coordination sphere of Ln ions in crystallographic non-equivalent positions for tetranuclear complexes of Dy **1(a,b)** and Yb **2(a,b)** and averaged for different types of oxygen atoms: O(s), O(t) and O(d). The reported distances correspond to crystallized complexes reported in Ref. [13].

$Yb_4(dbm)_4(O\text{-}btd)_6(OH)_2$		$Dy_4(dbm)_4(O\text{-}btd)_6(OH)_2$		$Yb_4(dbm)_6(O\text{-}btd)_4(OH)_2$		$Dy_4(dbm)_6(O\text{-}btd)_4(OH)_2$	
$Yb-\overline{X}$	d, Å	$Dy-\overline{X}$	d, Å	$Yb-\overline{X}$	d, Å	$Dy-\overline{X}$	d, Å
Yb_1-O_s	2.243	Dy_2-O_s	2.262	Yb_1-O_t	2.281	Dy_1-O_t	2.333
Yb_1-O_t	2.320	Dy_2-O_t	2.348	Yb_1-O_s	2.245	Dy_1-O_s	2.283
Yb_1-O_d	2.338	Dy_2-O_d	2.353	Yb_1-O_d	2.343	Dy_1-O_d	2.387
Yb_1-N_3	2.630	Dy_2-N_{31}	2.624	Yb_1-N	2.503	Dy_1-N	2.552
Yb_2-O_s	2.235	Dy_1-O_s	2.257	Yb_2-O_s	2.284	Dy_2-O_s	2.33
Yb_2-O_t	2.293	Dy_1-O_t	2.307	Yb_2-O_t	2.313	Dy_2-O_t	2.365
Yb_2-O_d	2.352	Dy_1-O_d	2.368	Yb_2-O_d	2.356	Dy_2-O_d	2.400
Yb_2-N	2.499	Dy_1-N	2.522				

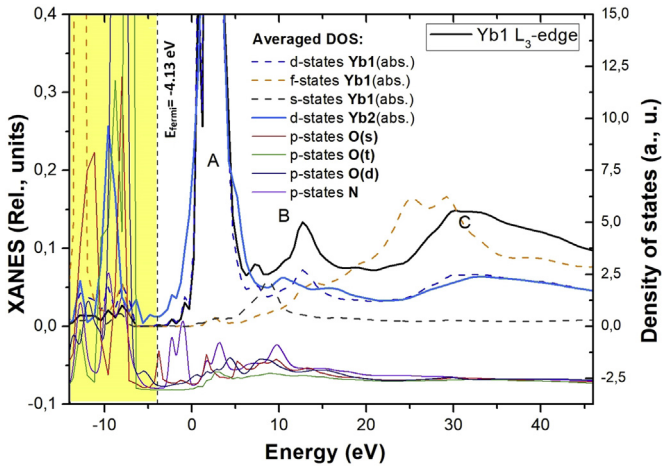

Fig. 7. Unconvoluted theoretical XANES spectra calculated for $Yb^{(1)}$ crystallographic position in the complex **1a** (values reported on the left scale) in comparison with partial density of states (DOS) for absorbing $Yb^{(1)}$ ion (reported as a dashed lines) and coordinated O and N atoms (shifted along vertical axis by −3 a.,u for clarity). *d*-DOS calculated for non-excited $Yb^{(2)}$ is reported for comparison. The lower energy part of the plot separated by yellow rectangle field corresponds to the occupied electronic states located below calculated Fermi energy of −4,13 eV.

$Yb^{(1)}$ position unconvoluted XANES spectra. The total density of unoccupied $Yb^{(1)}$ *s*-states having a peak at the energy of ~ 8.79 eV (or at 12.92 eV with respect to calculated Fermi energy) has not reflected in the theoretical $Yb^{(1)}$ XANES spectra. At this energy, a local minimum is observed (as well as a local minimum presented in a *d*-DOS of $Yb^{(1)}$). Thus, one can expect the only negligible effect of a possible dipole allowed ($\Delta l = \pm 1$) transition from excited 2*p* states to unoccupied 6*s* states. High density of *f*-unoccupied $Yb^{(1)}$ states has a double peak at 25.0 eV and 29.2 eV, which is obviously also not reflected in the theoretical $Yb^{(1)}$ XANES spectrum. This finding reveals that possible quadrupole transitions ($\Delta l = \pm 2$) from occupied 2*p* states to partially unoccupied 4*f* shell (for Yb^{+3}) is not observed in the simulated spectrum. It allows to draw a conclusion that there is no evidence of strong mixing between *p*- empty orbitals of ligand atoms (O, N) and *d*- empty orbitals of $Yb^{(1)}$ in the complex **1a**. The results of DOS calculations for $Yb^{(1)}$ of **2a** complex are reported at Figure S7 in Supplementary materials.

3.5. XANES simulations: comparison of finite difference method and multiple scattering theory approaches

In this section we have tested how different additional corrections affect the shape of the simulated XANES spectrum, also providing a comparison between the results obtained by full potential finite difference method (used for all the above presented simulations and denoted as “FDM” in this section) and multiple scattering theory based calculation (denoted as “MST” in this section) in a restricted muffin-tin potential (See Section 2.3).

Fig. 8 reports an unconvoluted XANES spectra simulations for $Yb^{(1)}$ crystallographic position calculated by both approaches with implementation of different additional corrections. First, it should be noted that in case of standard simulation mode (“normal mode” in the Fig. 8), MST approach result in more broadened peak C, and a very smooth even for the unconvoluted spectra feature B. However, in agreement with a previously reported MST based calculations for actinides and lanthanides [26], the implementation of MST is able to reproduce some of the pre-edge features, located at *ca.* 8940–8942 eV (the peak is emphasized with a * symbol in Fig. 8). The discussion of pre-edge feature in L_3-edges XANES spectra of Ln-complexes is beyond the scope of the present work. Afterwards XANES spectra have been simulated with implementation of self-consistent electronic density optimization (“SCF” in the Fig. 8) described in detail by Joly et al., [31]. In case of MST calculations, the implementation of SCF mode results in a minor change in the shape of features B and C, and disappearing of pre-edge contributions in

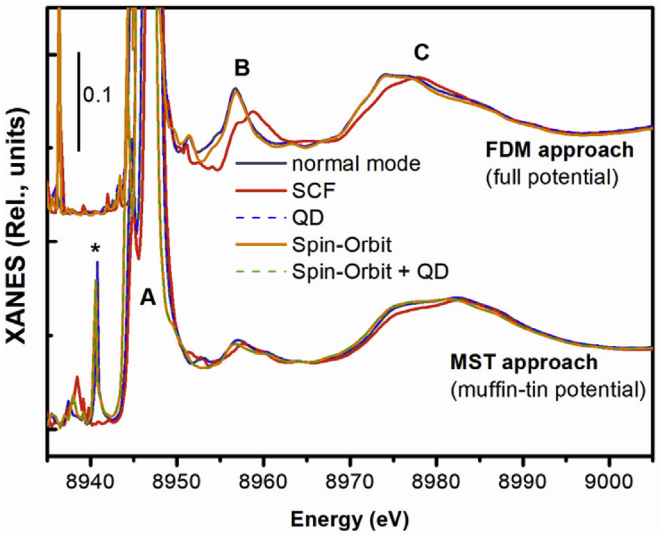

Fig. 8. Comparison of unconvoluted $Yb^{(1)}$ XANES spectra calculated for **1a** by FDM and MST approaches with a different additional corrections.

8940–8942 eV range of the spectra. Conversely in case of FDM approach SCF results in explicit energy shift of the features B and C towards the higher energy range, which is accompanied by the changes in the shape of these features. Thus implementation of SCF mode slightly improves the problem of energy gap (between WL peak and second maxima – peak C) underestimation, when a theoretical spectrum is compared with experimental one. On the next stage a quadrupole allowed transitions ($\Delta l = \pm 0,2$) as well as a spin-orbit coupling for the final states ("QD" and "Spin-Orbit" in the Fig. 8) have been taken into consideration. In both FDM and MST approaches these two additional corrections do not change the shape of the simulated spectra resulting only in minor changes in the pre-edge region. A combined implementation of QD and Spin-Orbit modes (simulated only in MST approach) does not result in any further changes of the spectra.

4. Conclusions

The local atomic structure similarity between recrystallized and as-synthesized samples of the Ln-complexes under the study has been proved by L_3-edge XANES spectroscopy. Differences in the experimental XANES spectra collected for a Ln-complexes with a different ligand ratio (dbm^-):($O\text{-}btd^-$) has been assigned with different abundancy of elongated Ln-N bonds with respect to Ln-O which results in delocalization of *d*- unoccupied states reflected in the simulated spectra.

It has been found that XANES simulations performed by FDMNES code underestimate the energy localization of the second absorption maxima, thus one should take it into account while fitting an experimental spectrum by varying a structural model. A further implementation of self-consistent optimization of the electronic structure slightly improve this problem. Consideration of quadrupole transitions as well as spin-orbit coupling of the final state do not affect significantly the shape of the simulated spectra both in case of finite difference method or multiple scattering theory approaches. Partial density of state calculations reveal that the shape of the XANES spectra mostly defined by the density of unoccupied *d*-states as well as lack mixing between unoccupied *p*-states of O and N atoms and *d*-states of Ln ions in the investigated complexes.

Since the product yield of as-synthesized Ln-complexes is significantly higher rather than after re-crystallization this work demonstrate a high potential of DFT-assisted XANES analysis for the structural investigation of as-synthesized complexes without long-range atomic ordering. Furthermore, advanced experimental studies with utilization of synchrotron radiation can be employed to perform more precise XANES analysis and EXAFS quantitative fitting. Also XMCD experiment can shed lights into magnetic properties of the materials on the atomic scale.

Acknowledgments

IAP, ANK and AVS acknowledge the Ministry of Education and Science of the Russian Federation for the award of Grant n. 16.3871.2017/4.6 ("Picometre diagnostics of parameters of 3D atomic structure of nanomaterials on the basis of XANES spectroscopy"). Authors are grateful to Kirill Lomachenko for providing assistance in experimental data acquisition by means of laboratory X-ray absorption spectrometer in Southern Federal University.

Appendix A. Supplementary data

Supplementary data to this article can be found online at https://doi.org/10.1016/j.molstruc.2019.03.073.

References

[1] S.V. Eliseeva, J.-C.G. Bünzli, Lanthanide luminescence for functional materials and bio-sciences, Chem. Soc. Rev. 39 (1) (2010) 189–227.
[2] C.P. Hauser, D.T. Thielemann, M. Adlung, C. Wickleder, P.W. Roesky, C.K. Weiss, K. Landfester, Luminescent polymeric dispersions and films based on oligonuclear lanthanide clusters, Macromol. Chem. Phys. 212 (3) (2011) 286–296.
[3] J. Tang, I. Hewitt, N.T. Madhu, G. Chastanet, W. Wernsdorfer, C.E. Anson, C. Benelli, R. Sessoli, A.K. Powell, Dysprosium triangles showing single-molecule magnet behavior of thermally excited spin states, Angew. Chem. 118 (11) (2006) 1761–1765.
[4] M.T. Gamer, Y. Lan, P.W. Roesky, A.K. Powell, R. Clérac, Pentanuclear dysprosium hydroxy cluster showing single-molecule-magnet behavior, Inorg. Chem. 47 (15) (2008) 6581–6583.
[5] J.-C.G. Bünzli, Lanthanide luminescence for biomedical analyses and imaging, Chem. Rev. 110 (5) (2010) 2729–2755.
[6] Q.Y. Zhang, X.Y. Huang, Recent progress in quantum cutting phosphors, Prog. Mater. Sci. 55 (5) (2010) 353–427.
[7] R. Sessoli, A.K. Powell, Strategies towards single molecule magnets based on lanthanide ions, Coord. Chem. Rev. 253 (19) (2009) 2328–2341.
[8] J. Luzon, R. Sessoli, Lanthanides in molecular magnetism: so fascinating, so challenging, Dalton Trans. 41 (44) (2012) 13556–13567.
[9] D.N. Woodruff, R.E.P. Winpenny, R.A. Layfield, Lanthanide single-molecule magnets, Chem. Rev. 113 (7) (2013) 5110–5148.
[10] P.C. Andrews, W.J. Gee, P.C. Junk, M. Massi, Variation of structural motifs in lanthanoid hydroxo clusters by ligand modification, New J. Chem. 37 (1) (2013) 35–48.
[11] T.S. Sukhikh, D.A. Bashirov, N.V. Kuratieva, A.I. Smolentsev, A.S. Bogomyakov, V.A. Burilov, A.R. Mustafina, A.V. Zibarev, S.N. Konchenko, New NIR-emissive tetranuclear Er(iii) complexes with 4-hydroxo-2,1,3-benzothiadiazolate and dibenzoylmethanide ligands: synthesis and characterization, Dalton Trans. 44 (12) (2015) 5727–5734.
[12] F.S. Mancilha, L. Barloy, F.S. Rodembusch, J. Dupont, M. Pfeffer, Cyclopalladated complexes of 4-aryl-2,1,3-benzothiadiazoles: new emitters in solution at room temperature, Dalton Trans. 40 (40) (2011) 10535–10544.
[13] T.S. Sukhikh, D.A. Bashirov, D.S. Kolybalov, A.Y. Andreeva, A.I. Smolentsev, N.V. Kuratieva, V.A. Burilov, A.R. Mustafina, S.G. Kozlova, S.N. Konchenko, Synthesis, luminescent and magnetic properties of new tetranuclear lanthanide complexes with 4-hydroxy-2,1,3-benzothiadiazolate and dibenzoylmethanide ligands, Polyhedron 124 (2017) 139–144.
[14] Frank de Groot, György Vankó, Pieter Glatzel, The 1s x-ray absorption pre-edge structures in transition metal oxides, J. Phys. Condens. Matter 21 (10) (2009), 104207.
[15] M. Centeno, P. Malet, I. Carrizosa, J. Odriozola, Lanthanide Doped V2O5/Al2O3 Catalysts: Structure-Activity Relationship in the, SCR of NOx, 2000.
[16] Kravtsova Antonina, Alexander A. Guda, Joerg Goettlicher, Alexander V. Soldatov, Vladimir K. Taroev, Anvar A. Kashaev, Lyudmila F. Suvorova, V.L. Tauson, Valence determination of rare earth elements in lanthanide silicates by L 3 -XANES spectroscopy, J. Phys. Conf. Ser. 712 (1) (2016), 012096.
[17] K.O. Kvashnina, S.M. Butorin, P. Glatzel, Direct study of the f-electron configuration in lanthanide systems, J. Anal. At. Spectrom. 26 (6) (2011) 1265–1272.

[18] C. Dallera, M. Grioni, A. Shukla, G. Vankó, J. L Sarrao, J.P. Rueff, D. Cox, New Spectroscopy Solves an Old Puzzle: the Kondo Scale in Heavy Fermions, 2002.
[19] C. Dallera, M. Grioni, A. Palenzona, M. Taguchi, E. Annese, G. Ghiringhelli, A. Tagliaferri, N.B. Brookes, T. Neisius, L. Braicovich, α-γ Transition in Metallic Ce Studied by Resonant X-Ray Spectroscopies, 2004.
[20] C. Dallera, O. Wessely, M. Colarieti-Tosti, O. Eriksson, R. Ahuja, B. Johansson, M. Katsnelson, E. Annese, J.-P. Rueff, G. Vankó, L. Braicovich, M. Grioni, Understanding Mixed Valent Materials: Effects of Dynamical Core-Hole Screening in High-Pressure X-Ray Spectroscopy, 2006.
[21] J.-P. Rueff, J.P. Itié, M. Taguchi, C. Hague, J.M. Mariot, R. Delaunay, J.P. Kappler, N. Jaouen, Probing the $\gamma - \alpha$ Transition in Bulk Ce under Pressure: A Direct Investigation by Resonant Inelastic X-Ray Scattering, 2006.
[22] A. Kotani, Unified Theory of X-Ray Magnetic Circular Dichroism at L-2,L-3 Absorption Edges for a Series of Ce Compounds, 2008.
[23] A. Soldatov, T.S. Ivanchenko, D. Longa S, A. Kotani, Y. Iwamoto, A. Bianconi, Crystal-structure Effects in the Ce L-III Edge X-Ray Absorption Spectrum of CeO2 Multiple Scattering Resonances and Many-Body Final States, 1994.
[24] A. Guda, S.A. Guda, K. Lomachenko, M. Soldatov, I.A. Pankin, A.V. Soldatov, L. Braglia, A. Bugaev, A. Martini, M. Signorile, E. Groppo, A. Piovano, E. Borfecchia, C. Lamberti, Quantitative Structural Determination of Active Sites from in Situ and Operando XANES Spectra: from Standard Ab Initio Simulations to Chemometric and Machine Learning Approaches, 2018.
[25] J.J. Rehr, J.J. Kas, M.P. Prange, A.P. Sorini, Y. Takimoto, F. Vila, Ab initio theory and calculations of X-ray spectra, Compt. Rendus Phys. 10 (6) (2009) 548–559.
[26] T. Vitova, M. Denecke, J. Goettlicher, K. Jorissen, J. Kas, K. Kvashnina, T. Prüßmann, J. Rehr, J. Rothe, Actinide and Lanthanide Speciation with High-Energy Resolution X-Ray Techniques, 2013.
[27] Y. Joly, X-ray absorption near-edge structure calculations beyond the muffin-tin approximation, Phys. Rev. B 63 (12) (2001), 125120.
[28] A. Tougerti, S. Cristol, E. Berrier, V. Briois, C. La Fontaine, F. Villain, Y. Joly, XANES study of rhenium oxide compounds at the L_1 and L_3 absorption edges, Phys. Rev. B 85 (12) (2012), 125136.
[29] O. Bunău, R.M. Galéra, Y. Joly, M. Amara, S.E. Luca, C. Detlefs, Resonant magnetic and multipolar scattering at the neodymium $L_{2,3}$ absorption edges in the antiferroquadrupolar phase of NdMg, Phys. Rev. B 81 (14) (2010), 144402.
[30] J.C. Slater, Phys. Rev. 51 (1937) 846–851.
[31] Y. Joly, O. Bunău, J.E. Lorenzo, R.M. Galéra, S. Grenier, B. Thompson, Self-consistency, spin-orbit and other advances in the FDMNES code to simulate XANES and RXD experiments, J. Phys. Conf. Ser. 190 (1) (2009), 012007.
[32] S.A. Guda, A.A. Guda, M.A. Soldatov, K.A. Lomachenko, A.L. Bugaev, C. Lamberti, W. Gawelda, C. Bressler, G. Smolentsev, A.V. Soldatov, Y. Joly, Optimized finite difference method for the full-potential XANES simulations: application to molecular adsorption geometries in MOFs and metal–ligand intersystem crossing transients, J. Chem. Theory Comput. 11 (9) (2015) 4512–4521.
[33] A. Bianconi, M. Dell Ariccia, A. Gargano, C.R. Natoli, EXAFS and Near Edge Structure I, Springer Series in Chemical Physics, 1983, pp. 57–61.
[34] W.J. Evans, Tutorial on the role of cyclopentadienyl ligands in the discovery of molecular complexes of the rare-earth and actinide metals in new oxidation states, Organometallics 35 (18) (2016) 3088–3100.
[35] A.Y. Andreeva, T.S. Sukhikh, S.G. Kozlova, S.N. Konchenko, Exchange interactions and XPS O1s spectra in polynuclear lanthanide complexes with dibenzoylmethanide and 4-hydroxy-2,1,3-benzothiadiazole, J. Mol. Struct. 1166 (2018) 190–194.